Geophysical Research Letters®

Tree Blow-Down by Snow Avalanche Air-Blasts: Dynamic Magnification Effects and Turbulence

Yu Zhuang[1,2] , Natalie Piazza[3] , Aiguo Xing[1] , Marc Christen[2,4], Peter Bebi[2,4], Alessandra Bottero[2,4], Lukas Stoffel[2,4], Julia Glaus[2,4], and Perry Bartelt[2,4]

[1]State Key Laboratory of Ocean Engineering, Shanghai Jiao Tong University, Shanghai, PR China, [2]WSL Institute for Snow and Avalanche Research SLF, Davos Dorf, Switzerland, [3]Department of Agricultural and Environmental Sciences, University of Milan, Milan, Italy, [4]Climate Change, Extremes and Natural Hazards in Alpine Regions Research Centre CERC, Davos Dorf, Switzerland

Abstract Snow avalanche-induced air-blasts are capable of breaking trees, damaging buildings and causing fatalities. Predicting their destructive properties is an essential part of snow avalanche hazard mitigation. Here, we propose a depth-averaged model that involves turbulent fluctuations to simulate the air-blast dynamics. The turbulent energy of the air-blast arises from that of dust-mixed air transferred from the avalanche core, shearing work in the cloud and entrained air, and is exploited to improve the air entrainment and drag relationships. We further present a unique data set of air blast-induced tree breakage, providing type, status, diameter and falling direction of the measured trees. Through case studies of two artificially released avalanches with measured powder heights and three natural avalanches with tree-breakage information, we test the model and investigate the turbulence effect on air-blast dynamics. The proposed model and tree-breakage data set quantify the air-blast destructiveness and can be applied for avalanche hazard assessment.

Plain Language Summary Snow avalanche-induced air-blasts are common natural hazards in high-altitude regions. They are fully turbulent mixtures of ice dust and gases capable of causing damage and human fatalities far beyond the avalanche deposits, representing a major threat to societies in avalanche-prone environments. In this study, we propose a robust numerical model that accounts for the turbulent fluctuations to simulate the air-blast dynamics. An unprecedented data set of air blast-induced tree breakage in three natural snow avalanches is further presented. Using five case studies in Switzerland, of which two artificial avalanches and three natural avalanches with tree-breakage data, we test the model and investigate the impact of turbulence on air-blast dynamics. Results suggest great performances of the proposed model in calculating the air-blast height, impact area and dynamic pressure. Turbulent fluctuations play an important role in the travel resistance and air entrainment of the air-blast, and can magnify the maximum pressure several times larger than the mean value. The new air-blast hazard model gives promising perspectives for estimations of snow avalanche hazards, and the tree-breakage data set can serve as a calibration basis for future more accurate numerical avalanche models.

1. Introduction

The prediction of the destructive potential of snow/ice avalanche air-blasts remains a major uncertainty in mountain hazard engineering (Eckerstorfer et al., 2016; Kargel et al., 2016; Schweizer, 2008). Powerful air-blasts can cause damage and fatalities well beyond the reach of the core, essentially expanding the hazard range of the avalanche (Stoffel et al., 2016; Zhuang, Xu, et al., 2023). This was the case of the devastating snow/ice avalanche of Langtang in which the village was situated outside the reach of the avalanche core but was destroyed by the air-blast (Fujita et al., 2017). Clearly, an engineering model that could predict the reach and magnitude of the air-blast in a real mountain topography would find wide application in natural hazard mitigation planning.

Although the danger of the air-blast is well known, and even included in existing snow avalanche mitigation guidelines (Stoffel et al., 2016), direct measurements of actual impact pressure are rare. Large, destructive events are both sudden and seldom, and preclude direct measurements of their inner structure. Hazard engineers are often interested in the force of the dust cloud, after it has decoupled from the core. In this situation, the momentum exchange between the core and cloud is fully complete and the cloud movement can best be described as an inertial flow (Sukhanov, 1982; Sukhanov & Kholobayev, 1982). The cloud is slowing by a combination of

Supervision: Aiguo Xing, Perry Bartelt
Validation: Yu Zhuang, Aiguo Xing, Peter Bebi, Lukas Stoffel, Julia Glaus
Visualization: Marc Christen
Writing – original draft: Yu Zhuang, Aiguo Xing, Perry Bartelt
Writing – review & editing: Yu Zhuang, Alessandra Bottero, Perry Bartelt

turbulent and laminar drag, both closely associated with the air entrainment. These processes are difficult to model and require measurement data to calibrate how the cloud dissipates its kinetic energy over time (Nishimura et al., 1995; Sovilla et al., 2018).

To date the best estimates of the air-blast power are based on tree-breakage observations (Bartelt et al., 2018b; Feistl et al., 2015; Zhuang, Xing, et al., 2023). Fallen trees indicate the spatial extent of avalanche-induced air-blast and create natural vector fields delineating their primary travel direction. In this paper we present an unprecedented data set of air blast-induced tree breakage. The measurements provide the type, status, DBH and falling direction of totally 488 trees in 17 forest plots, enabling testing hazard models in terms of the pressure and travel direction of the air-blast. The first goal of this paper is therefore to provide the snow/ice avalanche community with a unique data set to test both analytical and numerical air-blast models.

Over the past two decades, hazard engineers made numerous efforts to forecast the powder cloud movement. Early models were based on simple spherical cap approximations (Ancey, 2004; Turnbull et al., 2007). The cloud shape resembles a spherical cap, but these one-dimensional methods do not adequately model the formation phase involving the interaction with the core. As an alternative, recent efforts applied three-dimensional computational fluid dynamics (CFD) method to reproduce historical avalanches (Fei et al., 2022; Sampl & Granig, 2009; Zhuang, Xu, et al., 2023). These models appear to better capture the formation phase of the cloud dynamics, but their time-costs are excessive for engineering applications. Many three-dimensional approaches treat the air-blast as pure air, ignoring the ice-dust mass, leading to an underestimation of the air-blast pressure (Fei et al., 2022; Zhuang, Xu, et al., 2023).

Depth-averaged models present an alternative to one-dimensional analytical approaches, without requiring the computational resources of three-dimensional CFD models. They have been widely used to assess the avalanche air-blast hazard (Bartelt et al., 2016, 2018a; Turnbull & Bartelt, 2003). The depth-averaged model speeds-up the calculation since it reduces a three-dimensional problem to two-dimensions through integrating cloud properties perpendicular to the ground. It allows the model to consider some essential physical processes, such as mass/momentum exchanges between the core and cloud, air entrainment, cloud drag, and snow entrainment (Sovilla & Bartelt, 2002). Avalanche-induced air-blasts, however, are known to exhibit turbulent features (Ito et al., 2017; Ivanova et al., 2022), which contribute to their destructive power. The challenge lies in incorporating the formation and dissipation of turbulent structures within the depth-averaged framework. Significant gaps in understanding remain concerning how the turbulent fluctuations modify depth-averaged velocity profiles, pressure profiles and energy dissipation inside the cloud.

The second goal of this paper can now be stated. Using the measured tree-breakage data, we propose relationships to model cloud drag, air entrainment and decay of turbulence, and introduce these measurement-derived relationships into a depth-averaged avalanche model. Our goal is to show how the dissipation of kinetic energy, both laminar and turbulent, controls the air-blast magnitude. Five avalanches in Switzerland, including two avalanches released in the Vallée de la Sionne (VDLS) field site (No. 509 and No. 628) and three natural avalanches with the tree-breakage information, are analyzed for this purpose. Measurements in VDLS are used, since information regarding the release and entrainment mass, avalanche speed and powder height are known (Dreier et al., 2016; Veitinger & Sovilla, 2016).

2. Methods

2.1. Observed Tree Breakage

In January 2019, after a large snowfall, heavy orographic precipitation led to a level 5 avalanche danger (the highest danger; Meister, 1995) in the Canton of the Grisons, Switzerland. On 15 January 2019, the Salezer and Braemabuel South avalanches occurred in the Davos municipality and the Innerchinn avalanche occurred in the Klosters municipality. Information about the three avalanches is presented in Text S1 and Figures S1–S3 in Supporting Information S1.

Fieldwork was carried out from 16 April to 9 May 2019. We selected 17 study plots, including 5 plots in the Salezer avalanche, 6 plots in the Innerchinn avalanche and 6 plots in the Braemabuel South avalanche. Each circular plot covered an area of 314.16 m^2 (diameter 20 m). We measured trees with a diameter at breast height (DBH, 1.3 m height) or diameter at breaking point (DBP) $\geq$10 cm (totally 488 trees). For each tree we measured:

tree species, status (upright, fallen, leaning and stump), DBH/DBP and falling direction from north (for fallen and leaning trees). Tree measurement details are listed in Text S1, Tables S1–S3 and Figures S4–S6 in Supporting Information S1.

2.2. Tree-Breakage Calculation

The air-blast loading frequency is known to be similar to the tree eigenfrequency (Bartelt et al., 2018b). Hence, inertial forces, which would make trees easier to damage, must be considered. In this study, the determination of tree eigenfrequency ω refers to Zhuang, Xing, et al. (2023): modeling trees as Euler-Bernoulli beams and calculating the eigenfrequency according to the elastic theory. The frequency of air-blast loading derived from $\overline{\omega} = \pi/t_0$, t_0 is the loading duration calculated by the depth-averaged model. The inertial force effect is quantified by the magnification factor D, defined as (Bartelt et al., 2018b):

$$\begin{cases} D = \frac{1}{1-\beta^2}\left[\sin\left(\frac{2\pi\beta}{\beta+1}\right) - \beta\sin\frac{2\pi}{\beta+1}\right] & \beta < 1 \\ D = \frac{\pi}{2} & \beta = 1 \\ D = \frac{2\beta}{\beta^2-1}\cos\frac{\pi}{2\beta} & \beta > 1 \end{cases} \tag{1}$$

where $\beta = \overline{\omega}/\omega$ is the ratio between the air-blast loading frequency and tree eigenfrequency. The tree-breakage assessment is applied according to Feistl et al. (2015):

$$\sigma_\Pi = D \cdot c_\Pi \rho_\Pi \frac{8u_\Pi^2}{\pi d^3} w H^2 \cos\gamma \tag{2}$$

where c_Π is drag coefficient, u_Π is air-blast velocity, d is stem diameter, H is tree height, w is effective crown width, γ is slope angle. Tree species in the calculation is Norway spruce and the stem diameter is the measured average value in the plot. Tree height is estimated from stem diameter based on the measurements by Jonsson et al. (2006). c_Π and w are experienced values. The breakage occurs when the bending stress σ_Π exceeds the experienced tree strength.

2.3. Turbulent Depth-Averaged Avalanche Model

2.3.1. General Framework

We propose a turbulent, depth-averaged model to simulate the flow dynamics of the snow/ice avalanche. The avalanche core Φ and the cloud Π are separated into two different layers, Figure 1 (Bartelt et al., 2016). The core is a granular, gravity-driven shear flow that can disperse and compress. The dispersive movement of the snow/ice particles allows both the intake and expulsion of air, now loaded with ice-dust that becomes loose during particle interactions, or when the core impacts and entrains the snowcover. The net effect of the interaction is to transfer mass/momentum from the core to cloud and creates turbulent structure in the cloud. The cloud is therefore modeled as a turbulent suspension of ice-dust that is driven by gravity, and momentum and turbulence supplied by the core. The depth-averaged model predicts both the mean velocity and density of the cloud, as well as velocity fluctuations. From these values the air-blast pressure can be found.

2.3.2. Avalanche Core Φ

To model the avalanche core, we apply the general model developed by Bartelt et al. (2006, 2016); Buser and Bartelt (2009, 2011, 2015) for mixed flowing/powder avalanche flow. The model includes entrainment (Bartelt et al., 2018c), forest interaction (Feistl et al., 2015) and thermal processes of snow melting (Valero et al., 2015). The core movement is described by three state variables, the so-called co-volume height $\hat{h}_\Phi$, the flowing height h_Φ and the slope-parallel velocity $\vec{u}_\Phi$. The co-volume represents the snow packing in the deposition zone and is given by the co-volume density $\hat{\rho}_\Pi$ (Bartelt & McArdell, 2009). The governing equations for the core are:

$$\left(\hat{h}_\Phi\right)_t + div\left(\hat{h}_\Phi\vec{u}_\Phi\right) = \frac{\rho_\Sigma}{\hat{\rho}_\Phi}\dot{M}_{\Sigma\to\Phi} - \dot{M}_{\Phi\to\Psi} - \frac{\hat{\rho}_\Pi}{\hat{\rho}_\Phi}\dot{M}_{\Phi\to\Pi} \tag{3}$$

$$\left(h_\Phi\right)_t + div\left(h_\Phi\vec{u}_\Phi\right) = \mathbb{D}\left(t, k_z, \dot{k}_z, \ddot{k}_z\right) \tag{4}$$
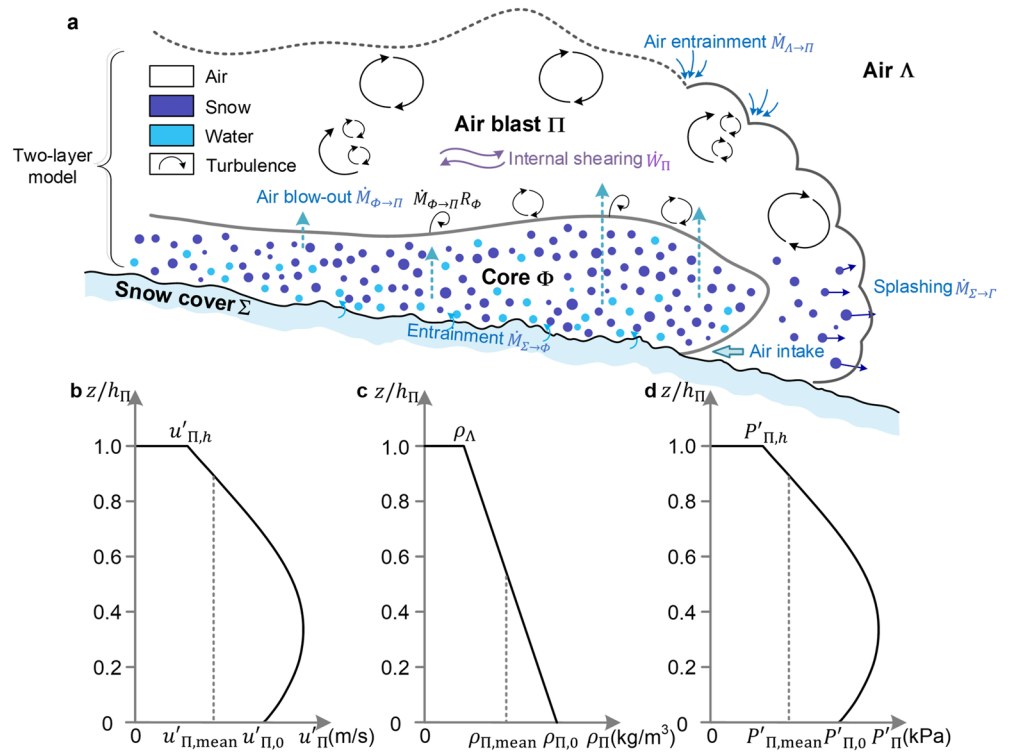
Figure 1. (a) Schematic diagram of a snow avalanche air-blast system. Panels (b)–(d) describe the assumed air-blast profile of the turbulent velocity, powder density and turbulent pressure, respectively.

$$\left(\hat{h}_\Phi \vec{u}_\Phi\right)_t + div\left(\hat{h}_\Phi \vec{u}_\Phi \otimes \vec{u}_\Phi + p_\Phi I\right) = \vec{G}\hat{h}_\Phi - \frac{\vec{u}_\Phi}{\|\vec{u}_\Phi\|}\left[S_\Phi(R_\Phi, T_\Phi, m_\Phi)\right]$$
$$- \left[(1 + r_\Gamma)\frac{\rho_\Sigma}{\hat{\rho}_\Phi}\dot{M}_{\Sigma\to\Gamma} + \dot{M}_{\Phi\to\Psi} + \frac{\hat{\rho}_\Pi}{\hat{\rho}_\Phi}\dot{M}_{\Phi\to\Pi}\right]\vec{u}_\Phi \tag{5}$$

$$\left(\hat{h}_\Phi R_\Phi\right)_t + div\left(R_\Phi \hat{h}_\Phi \vec{u}_\Phi\right) = \alpha_\Phi \dot{W}_\Phi + \varepsilon_\Phi \rho_\Sigma \dot{L}_{\Sigma\to\Phi} - \dot{M}_{\Phi\to\Pi} R_\Phi - \beta_\Phi \hat{h}_\Phi R_\Phi \tag{6}$$

$$\left(\hat{h}_\Phi E_\Phi\right)_t + div\left(E_\Phi \hat{h}_\Phi \vec{u}_\Phi\right) = [1 - \alpha_\Phi]\dot{W}_\Phi + \beta_\Phi \hat{h}_\Phi R_\Phi + [1 - \varepsilon_\Phi]\rho_\Sigma \dot{L}_{\Sigma\to\Phi} + \rho_\Sigma c_\Sigma T_\Sigma \dot{M}_{\Sigma\to\Phi} - E_\Phi \dot{M}_{\Phi\to\Pi} - \dot{Q}_m \tag{7}$$

$$S_\Phi = \mu_\Phi(R_\Phi, T_\Phi, m_\Phi)N_\Phi + \rho_\Phi g \frac{u_\Phi^2}{\xi_\Phi(\rho_\Phi, T_\Phi, w_\Phi)} \tag{8}$$

$$\dot{L}_\Sigma = \dot{L}_{\Sigma\to\Phi} + \dot{L}_{\Sigma\to\Gamma} = \underbrace{\frac{1}{2}(1 - \gamma_\Gamma)\dot{M}_\Sigma u_\Phi^2}_{\dot{L}_{\Sigma\to\Phi}} + \underbrace{\frac{1}{2}\gamma_\Gamma\left(1 - r_\Gamma^2\right)\dot{M}_\Sigma u_\Phi^2}_{\dot{L}_{\Sigma\to\Gamma}} = \frac{1}{2}\left[1 - \gamma_\Gamma r_\Gamma^2\right]\dot{M}_\Sigma u_\Phi^2 \tag{9}$$

$$(m_\Phi)_t + div\left(m_\Phi \vec{u}_\Phi\right) = \frac{\dot{Q}_m}{[\rho_w L]} \tag{10}$$

$$\int_0^{\Delta t} \dot{Q}_m dt = \rho_w c_\Phi h_\Phi [T_\Phi - T_m] \tag{11}$$

Equations 3 and 5 are the mass and momentum balances, which involve the avalanche entrainment $\dot{M}_{\Sigma\to\Phi}$, forest interaction $\dot{M}_{\Phi\to\Psi}$, and mass/momentum transfer to the cloud $\dot{M}_{\Phi\to\Pi}$. Equation 4 describes the dilution and compression of the core. $\mathbb{D}\left(t, k_z, \dot{k}_z, \ddot{k}_z\right)$ represents the change in core height due to dispersive pressure effects (Bartelt et al., 2016). Equations 6 and 7 describe the balance of the fluctuation energy and heat energy. Shearing S_Φ is controlled by the process-based Voellmy rheology (Salm, 1993, Equation 8, parameters $<\mu_\Phi, \xi_\Phi>$, normal stress

N_Φ). The total dissipative energy flux $\dot{L}_\Sigma$ is defined in Equation 9 and accounts for the avalanche energy lost during entrainment. Snowcover is not only entrained but accelerated forward to create splashing pre-fronts (parameters $<\gamma_\Gamma, r_\Gamma>$, Bartelt et al., 2018c). Equation 10 describes the production and transport of meltwater. We note the mean avalanche temperature T_Φ never exceeds the snow melting temperature T_m, therefore define latent heat energy dQ_m as Equation 11 (latent heat L). The parameters $(\alpha_\Phi, \varepsilon_\Phi)$ split the shearing process $\dot{W}_\Phi = S_\Phi \|\vec{u}_\Phi\|$ and dissipative energy flux of entrainment $\dot{L}_{\Sigma \to \Phi}$ into fluctuation energy R_Φ and internal energy E_Φ (Bartelt et al., 2006). The model parameters are described in Bartelt et al. (2016, 2018c) and listed in Table S4 in Supporting Information S1.

2.3.3. Powder Cloud Π

The powder cloud Π is simulated by equations of mass (Equations 12 and 13) and momentum balance (Equation 14), and additional equations associated with the production and decay of turbulent fluctuations (Equation 15):

$$\left(\hat{h}_\Pi\right)_t + div\left(\hat{h}_\Pi \vec{u}_\Phi\right) = \dot{M}_{\Phi \to \Pi} \tag{12}$$

$$(h_\Pi)_t + div\left(h_\Pi \vec{u}_\Pi\right) = \frac{\rho_i - \hat{\rho}_\Pi}{\rho_i - \rho_\Lambda} \dot{M}_{\Phi \to \Pi} + \dot{M}_{\Lambda \to \Pi} \tag{13}$$

$$\left(\hat{h}_\Pi \vec{u}_\Pi\right)_t + div\left(\hat{h}_\Pi \vec{u}_\Pi \otimes \vec{u}_\Pi + p_\Pi I\right) = \frac{(\hat{\rho}_\Pi - \rho_\Lambda)}{\hat{\rho}_\Pi} \vec{G} \hat{h}_\Pi + \dot{M}_{\Phi \to \Pi} \vec{u}_\Phi - \frac{\vec{u}_\Pi}{\|\vec{u}_\Pi\|} S_\Pi - \frac{\rho_\Lambda}{\hat{\rho}_\Pi} \dot{M}_{\Lambda \to \Pi} \vec{u}_\Pi \tag{14}$$

$$\left(\hat{h}_\Pi R_\Pi\right)_t + div\left(R_\Pi \hat{h}_\Pi \vec{u}_\Pi\right) = \dot{W}_\Pi + \dot{M}_{\Phi \to \Pi} R_\Phi + \frac{1}{2} \rho_\Lambda \dot{M}_{\Lambda \to \Pi} u_\Pi^2 - \beta_\Pi \hat{h}_\Pi R_\Pi \tag{15}$$

Similar to the core, $\hat{h}_\Pi$ represents the initial cloud height, corresponding to the initial cloud density $\hat{\rho}_\Pi$ before blowing out from the core; $\hat{h}_\Pi$ is related to the downward z-displacement of the core and driven by compression/expansion of the granular ensemble (Equation 4, Bartelt et al., 2016); h_Π represents the true cloud height affected by clouds ejected from the core $\dot{M}_{\Phi \to \Pi}$ and air entrainment $\dot{M}_{\Lambda \to \Pi}$. Because of this air entrainment, the cloud density decreases to ρ_Π, satisfying $\rho_\Pi = \rho_i \frac{\phi_i \hat{h}_\Pi}{h_\Pi + \phi_i \hat{h}_\Pi} + \rho_\Lambda \frac{h_\Pi}{h_\Pi + \phi_i \hat{h}_\Pi}$, $\rho_i = 971$ kg/m^3 is the ice density, $\rho_\Lambda = 1.225$ kg/m^3 is the air density and $\phi_i = \frac{\hat{\rho}_\Pi - \rho_\Lambda}{\rho_i - \rho_\Lambda}$ represents the ice fraction in the initial cloud. The cloud is driven by the momentum transferred from the core $\dot{M}_{\Phi \to \Pi} \vec{u}_\Phi$, and gravity $\frac{(\rho_\Pi - \rho_\Lambda)}{\rho_\Pi} \vec{G}$. In general, we find $\dot{M}_{\Phi \to \Pi} \vec{u}_\Phi \gg \frac{(\rho_\Pi - \rho_\Lambda)}{\rho_\Pi} \vec{G}$.

A unique feature of the model is the inclusion of turbulence (Gorynina & Bartelt, 2023). The instantaneous air-blast velocity $\tilde{u}_\Pi$ is integrated as a mean $\vec{u}_\Pi$ and a fluctuating component $\vec{u}_\Pi'$:

$$\tilde{u}_\Pi = \vec{u}_\Pi + \vec{u}_\Pi' = \langle u_x + u_x'(t), u_y + u_y'(t), u_z + u_z'(t) \rangle \tag{16}$$

where x,y,z represents the directions. The turbulent energy $R_\Pi(x,y,z,t)$ attributes to the velocity fluctuation is represented as (Richard & Gavrilyuk, 2012, 2013):

$$R_\Pi(x, y, z, t) = \frac{\hat{\rho}_\Pi}{2}\left[u_x'^2(t) + u_y'^2(t) + u_z'^2(t)\right] = \frac{\hat{\rho}_\Pi}{2} u_\Pi'^2(t) \tag{17}$$

The velocity fluctuation is assumed to be isotropic (Carroll & Blanquart, 2013) so that $R_{\Pi,x} = R_{\Pi,y} = R_{\Pi,z} = \frac{1}{3} R_\Pi$. The fluctuation energy is produced by three sources (Equation 15): fluctuation energy transferred from the core $\dot{M}_{\Phi \to \Pi} R_\Phi$, internal shearing $\dot{W}_\Pi = [\hat{\rho}_\Pi S_\Pi] \|\vec{u}_\Pi\|$ and air entrainment $\frac{1}{2} \rho_\Lambda \dot{M}_{\Lambda \to \Pi} u_\Pi^2$. β_Π is the parameter that controls the decay, and therefore the lifetime, of the fluctuation energy $-\beta_\Pi \hat{h}_\Pi R_\Pi$.

In the model, the air entrainment $\dot{M}_{\Lambda \to \Pi}$ and powder drag S_Π relationships are composed of both laminar and turbulent parts. Air entrainment is suggested as a function of the turbulent velocity ($\sqrt{R_\Pi}$), see (Turnbull & McElwaine, 2007): $\dot{M}_{\Lambda \to \Pi} = \alpha_L(\psi)(\rho_\Pi - \rho_\Lambda) + \alpha_T(\psi)\sqrt{R_\Pi \hat{h}_\Pi}(\rho_\Pi - \rho_\Lambda)$. The drag is suggested as a function of the turbulent energy: $S_\Pi = \mu_L(\zeta) u_\Pi + \mu_T(\zeta) R_\Pi \hat{h}_\Pi$. (α_L, α_T) and (μ_L, μ_T) are sets of laminar/turbulent parameters governing air entrainment and drag. The governing equations, for both the core and the cloud, are numerically solved using well-established finite volume schemes within the RAMMS software (Christen et al., 2010).

2.3.4. Vertical Profile of the Air-Blast Pressure

We assume the turbulent energy at the cloud top ($z = h_\Pi$) arises primarily from air entrainment. The upper surface of the cloud is a permeable boundary with atmosphere, where the ambient air is entrained into the

cloud (Andrews, 2014; Issler, 1998). We use the ratio of the entrainment energy to total turbulent energy $\theta_h = \frac{1}{2}\dot{M}_{\Lambda\rightarrow\Pi}u_\Pi^2/\dot{P}_\Pi$ to define the turbulence at the cloud top $R_\Pi(z = h_\Pi) = \frac{\theta_h}{3}R_\Pi$. Similarly, the source of turbulent energy at the lower surface ($z = 0$) is regarded to arise from the turbulent energy transferred from the core and shearing work. The ratio of this energy to total turbulent energy $\theta_0 = (\dot{M}_{\Phi\rightarrow\Pi}R_\Phi + \dot{W}_\Pi)/\dot{P}_\Pi$ is defined to describe the turbulence at the cloud bottom $R_\Pi(z = h_\Pi) = \frac{\theta_0}{3}R_\Pi$. The velocity fluctuations at the upper($u'_{\Pi,h}$) and lower surfaces($u'_{\Pi,0}$) are then calculated using Equation 17. According to field observations, the velocity profile is assumed to follow the parabolic form: $u'_\Pi(z) = az^2 + bz + c$ (Figure 1b). The coefficients are determined using the boundary values ($u'_{\Pi,0}$; $u'_{\Pi,h}$) and the mean value (Equation 15). The total pressure profile is thus written as $p(z) = \frac{1}{2} \cdot \rho_\Pi(z) \cdot u_\Pi(z)^2 = \frac{1}{2} \cdot \rho_\Pi(z) \cdot \left[\bar{u}_\Pi(z) + u'_\Pi(z)\right]^2$. A linear density profile $\rho_\Pi(z)$ is suggested considering the decreasing density from the bottom to the top of the cloud (Hermann & Hutter, 1991) (Figure 1c). The calculated pressure profile combined with the implemented tree-breakage assessment method (Section 2.2) can calculate the tree bending stress. Modeling parameters for the avalanche cases are calibrated and listed in Table S5 in Supporting Information S1.

3. Results

3.1. Model Validation From Core Velocity and Powder Height

The No. 509 and 628 avalanches are artificially released at the VDLS field site in Switzerland in 2003 and 2004, respectively (Veitinger & Sovilla, 2016). We tested the core velocity along a longitudinal profile and the powder height at monitoring points using video footage, providing the opportunity to test the proposed hazard model. Details of the measurement are presented in Dreier et al. (2016).

Figures 2a and 2b show the simulated air-blast dynamics of the two avalanches. The calculated air-blast pressure reaches far beyond the core deposits. The calculated maximum velocity of No. 509 and 628 avalanches reaches 53 m/s and 50 m/s, respectively. The simulated velocity evolution and measured values are highly similar with only slight deviations (Figures 2c and 2d). For the powder heights, the modeled results are in the same order of magnitude as the measurements (Figures 2e and 2f). The cloud height reaches the peak value within a few seconds after initiation with oscillatory fluctuations. Horizontal time deviations between the modeled and measured results arise from the error of the calculated core velocities. A model assumption is that the fracture slab has completely granularized after release. The slab break-up process is not modeled. At locations next to the release area (MP1 and MP4), the core has not completely fluidized, leading to an overestimation of the interstitial pore space between granules and subsequently a difference between the calculated and observed powder heights. We acknowledge that the exact shape of the turbulent cloud is unpredictable in both time and space. The proposed model is designed to predict air-blast pressures and maximum cloud heights for engineering calculations.

3.2. Turbulence-Enforced Air-Blast Dynamics

Regarding the fully turbulent structure of air-blasts, it is interesting to investigate the impacts of turbulence on air-blast dynamics. Parametric analysis of the turbulence decay coefficient β_Π is applied to the No. 628 avalanche. Modeling results suggest that a larger β_Π leads to a longer propagation distance (Figure 2g) but a lower powder height (Figure 2h). In the proposed model, we defined the drag and air entrainment as functions of turbulent energy. Therefore, the amount of turbulent energy is related to the moving resistance and volume of entrained air. In the case of a low β_Π value ($\beta_\Pi = 0.2$), the concentrated turbulent energy leads to a high drag resistance after the air-blast initiation, so that the generated air-blast loses momentum within a short duration and shows a short extent. However, air entrainment attributed to the turbulence arises in a powder height of over 70 m, ~1.5 times the actual condition. In the case of a high β_Π value ($\beta_\Pi = 5$), after the rapid dissipation of turbulent fluctuations, the cloud propagation is controlled by the low laminar drag, moving slowly to long distances with a low height.

Figure 2i shows the impact of turbulence on the dynamic pressure. The total pressure can be several times larger than that arises from the mean velocity, indicating the great importance of turbulence. In the case of $\beta_\Pi = 1$, the best-fitted value, the maximum pressure at the cloud bottom reaches 1.8 kPa, nearly twice the mean value. However, in the case of a small β_Π ($\beta_\Pi = 0.2$, unrealistic), the maximum pressure at the cloud bottom is 1.7 kPa, almost six times the mean pressure.
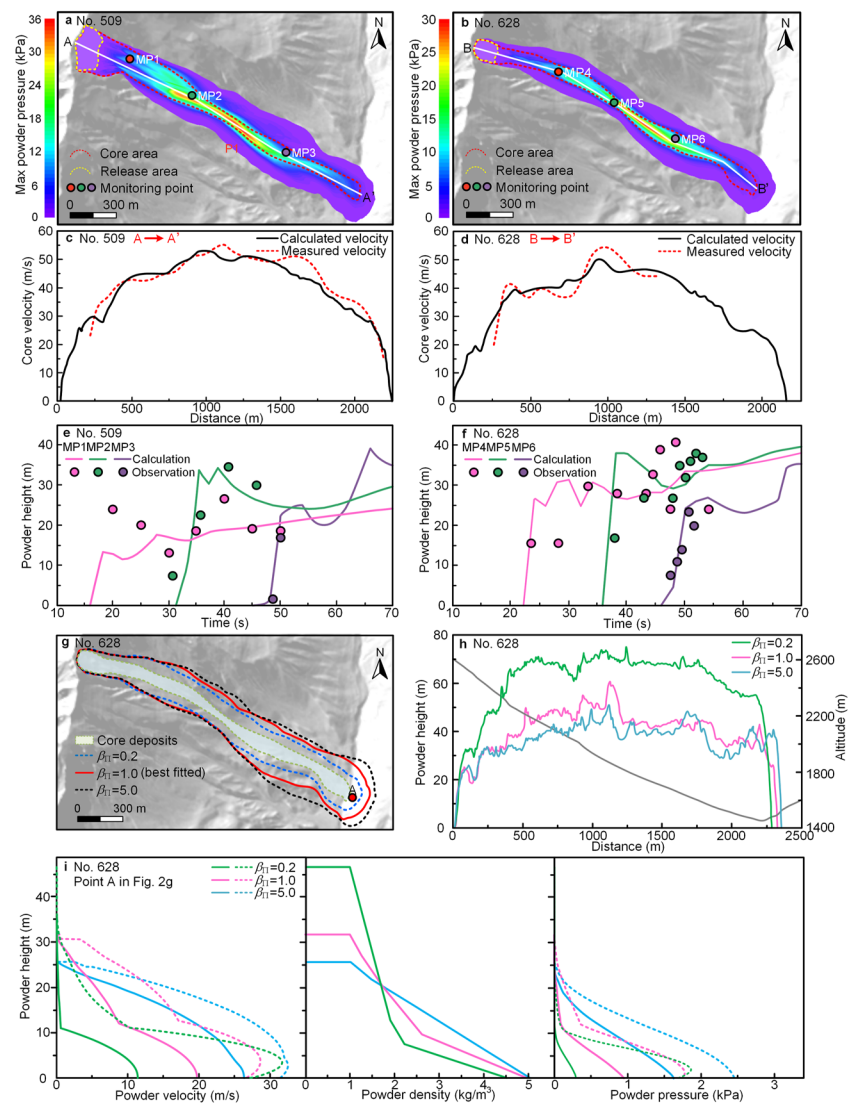
Figure 2. (a)–(b) Simulated air-blast pressure (arise from mean velocity) of the No. 509 and 628 avalanches and the locations of monitoring points. (c)–(d) Comparison between the calculated core velocity with measurements. (e)–(f) Comparison between the calculated powder height with measurements. The measured powder height has an error of ± 5 m. (g)–(i) Impacts of turbulence decay coefficient β_{Π} on the impact area, height and pressure of the air-blast, respectively. In panel (i), solids lines represent the air-blast pressure attribute to the mean velocity and dotted lines represent the total pressure attribute to both mean velocity and turbulent fluctuations.

3.3. Air Blasts-Induced Tree Breakage

Tree breakage outlines the impact area and travel direction of the air-blast, providing information to estimate the air-blast pressure. Figure 3 shows the calculated results of the three natural avalanches and plot locations. Modeling results of the core and air-blasts are validated through comparing with the observed deposit area and tree-breakage area. In the Salezer and Innerchinn avalanches, most plots (P1-P9) are located outside the core deposits, so the tree breakage results from the air-blast loading. Measured forest destruction in the Braemabuel South avalanche is in the avalanche travel path. The core and air-blasts jointly cause the forest destruction.

Similar to the No. 509 and 628 avalanches, air-blasts of all three cases show a larger impact area than core, in terms of both the longitudinal travel distance and the width (Figure 3). Modeled air-blast pressure in the longitudinal profiles indicates an increase in the initial stage and a subsequent fluctuation (Figures 3c, 3h, and 3m). Air-blasts arise from the avalanche core. Therefore, high powder pressure occurs at places with sudden terrain changes. Modeling results in the cross-sections indicate high powder pressure above the core (Figures 3d, 3i,
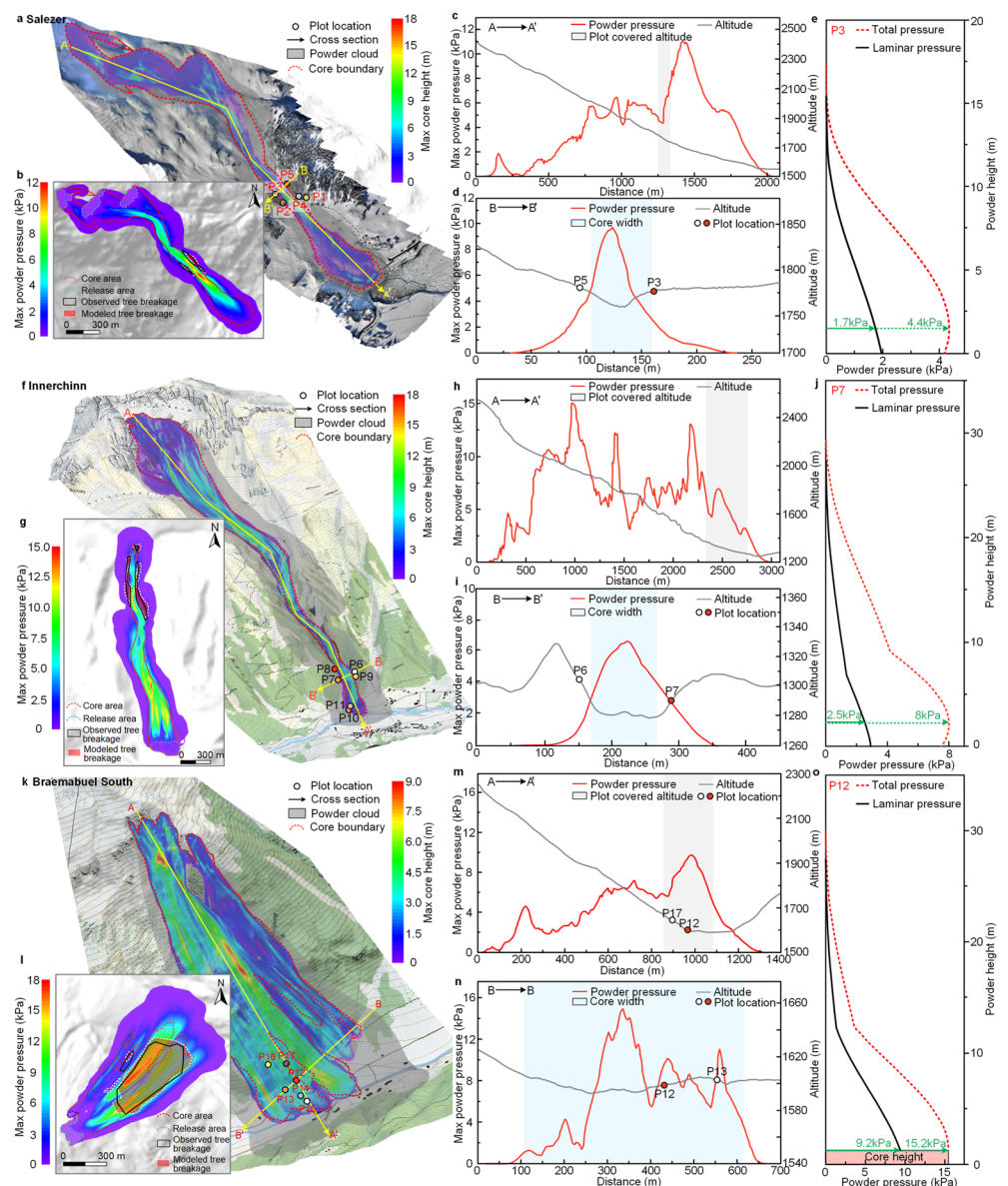
Figure 3. Air-blast dynamics of the three natural avalanches and the location of measured plots. Panels (a)–(e), (f)–(j), and (k)–(o) show the simulated maximum core height, maximum powder pressure contour, powder pressure evolution in the longitudinal profile and cross-section of each case, powder pressure profile at specific points, respectively. Gray shadows in the longitudinal profiles indicate the plot-covered altitude. Blue shadows in the cross-sections indicate the core width, showing the extent of air-blasts.

and 3n). Deep pressure gradients are observed near the core boundary, making the air-blast pressure drops to a low value after a short extent. Furthermore, the turbulent fluctuation greatly magnifies the dynamic pressure in all three cases (Figures 3e, 3j, and 3o). Especially in the Salezer and Innerchinn avalanches, the total powder pressure is over two times that attribute from the mean velocity at plots outside the core deposits.

The status and mean DBH of trees in each spot are presented in Figures 4a and 4b. Two key factors in quantifying air-blast risk are estimates of the dynamic pressure and loading direction. To test the proposed model with the measured tree-breakage data, we calculate the air-blast and core dynamics, and the associated tree-bending stress at the center of each plot (Table S6 in Supporting Information S1). Modeling results indicate tree breakage in 15 plots. Trees in Plot 1 and 2 in the Salezer avalanche remain upright, basically matching the measurements. Notably, the calculated tree bending stress in Plot 3 is 75.7 MPa, close to the experienced bending strength (72 MPa). This phenomenon explained observations that only half trees were damaged by the air-blast loading.
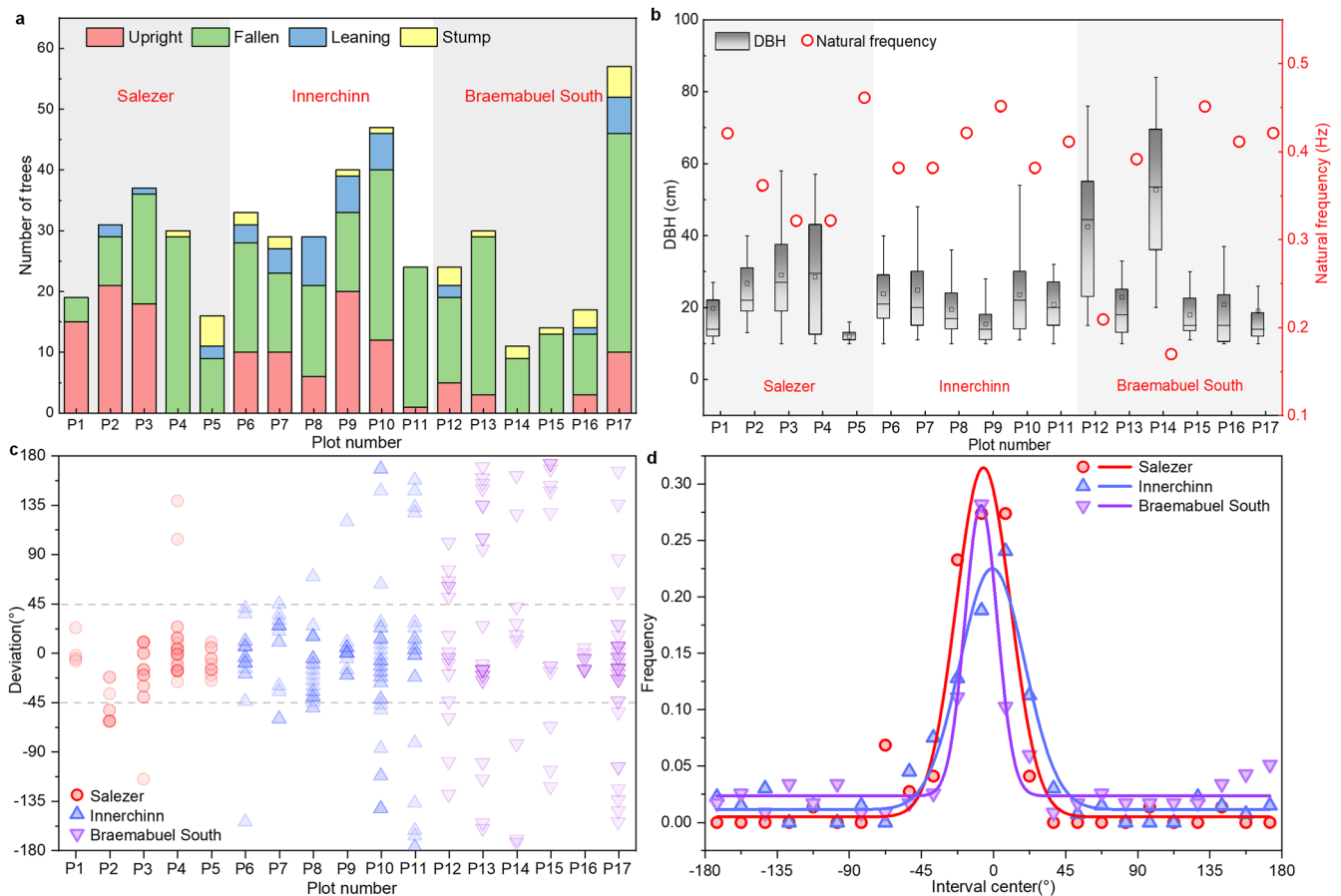
Figure 4. (a) Status of trees in each plot. (b) Average DBH and eigenfrequency of trees in each plot. The eigenfrequency is calculated using the average DBH. (c) Direction deviation of fallen/leaning trees. Dark colors represent overlapping data. (d) Frequency distribution of the direction deviations. The lines represent Gauss fits in different cases.

Figures 4c–4d shows the deviation of the calculated cloud moving direction with the measured tree falling directions. The falling directions of trees present a symmetrical distribution along the air-blast moving direction. Among the 326 fallen/leaning trees, the direction deviations of 241 trees list within 45°, accounting for 74% of the total amount. Dynamic response and breakage of trees subjected to air-blasts are complex due to the impacts of tree interaction and topography, thus leading to direction deviations. Interestingly, for plots affected by the avalanche core (P10-P11 in Innerchinn avalanche, P12-17 in Braemabuel South avalanche), tree falling directions show certain dispersivity, even some trees fell in the opposite direction with air-blasts. This is an indication of intense impact pressures near the ground, causing the trees to fall against the avalanche. Furthermore, 78% of the measured trees are in the fallen/stump status, but this percentage becomes 52% in P1-P9. The front of air-blast is known to move faster than the core and can destroy the trees before the core arrives. Therefore, we suggest the forests are primarily destroyed by the air-blast, but the subsequent avalanche flow can also destroy the remaining standing trees. The complex intermittent structure in the core and the rough terrain jointly changed the direction of some fallen trees. The core intensifies the extent of tree breakage and leads to the deviation of tree falling directions.

4. Discussion and Implications

With this contribution we supply a data set of powder avalanche air-blast tree breakage. We show that risk assessment of snow and ice avalanche air-blasts involves impact area, dynamic pressure and loading direction. This information can be used to quantify the attenuation of the powder cloud velocity involving both laminar/turbulent air-entrainment and drag. As comparable data sets are scarce, the publicly available tree-breakage data

set allows for the evaluation of existing air-blast models and can serve as a calibration basis for future, more robust air-blast models, ultimately leading to more accurate hazard assessment for societies in snow avalanche prone environments.

We have updated a depth-averaged mixed flowing/powder avalanche model to include the turbulent energy associated with velocity fluctuations in the cloud. Originally proposed by Russian scientists (Bozhinskiy & Losev, 1998), depth-averaged cloud models offer a middle way between simple, analytical spherical cap models (Ancey, 2004), and more complex three-dimensional CFD approaches (Zhuang, Xu, et al., 2023). Using the proposed model, we explored the magnification effects of turbulence on the air-blast pressure. The maximum air-blast pressure could exceed the mean values (arises from the mean velocity), which are commonly esti-mated for avalanche hazard assessments, by a factor of 2–4. According to practical experience in Switzerland (BFF/SLF, 1984), a pressure threshold of 3 kPa is suggested for air-blast hazard mapping. This implies a mean dynamic pressure of 1 kPa might be accompanied by a maximum pressure exceeding the threshold of 3 kPa, caus-ing potential damage to the surrounding forests and infrastructure. Similar conclusions are experimentally found in pyroclastic surges (Brosch et al., 2021), which suggested the maximum pressure arises from the turbulence is at least three times the mean values. Notably, the turbulent velocity profile we assume is in the same direction as the mean velocity, indicating the most dangerous scenario. The air-blast hazard is overestimated in some places. However, according to the powder avalanche measurements (Sovilla et al., 2018), spikes of maximum pressure are not local but appear almost simultaneously over a large part of the flow depth. Our modeling of the most dangerous scenario is therefore a necessary precaution for the air-blast hazard assessment.

Although we apply a depth-averaged model to analyze our data set of tree breakage, the proposed air-entrainment and drag functions can help the development of all future modeling approaches. The cloud drag controls the air-blast propagation, while the entrained air increases the powder height (Turnbull & McElwaine, 2007). In previous air-blast models, though scientists recognized the influence of turbulence, the drag and air entrainment relationships are established as functions of the mean velocity (e.g., Bartelt et al., 2016). Both mechanisms are highly related to turbulent fluctuations and are influential to the destructive potential of air-blasts. An important parameter becomes the rate of turbulent dissipation in the cloud (in our model β_Π). We quantify this parameter using the measured powder height and spatial extent of the observed tree-breakage. We recognize that more direct measurements are appropriate, and our results can only serve as a first, rough quantification for avalanche risk assessment.

Through modeling analysis of five avalanches, the air-blast modeling parameters are calibrated and are now listed within a comparatively small scope (Table S5 in Supporting Information S1). Practitioners can conduct the avalanche-air blast hazard mapping with the proposed model and parameters. Further case studies will help quantify the modeling parameters of air-blasts with less uncertainty. The present work is not only relevant for snow avalanche air-blasts, but for other particle-laden gravity currents, including pyroclastic surges (Brosch et al., 2021) and air-blasts triggered by ice/rock avalanches (Zhuang, Xu, et al., 2023).

Conflict of Interest

The authors declare no conflicts of interest relevant to this study.

Data Availability Statement

Data used in this study is available at Zhuang (2023a). The software is available at Zhuang (2023b).

References

Ancey, C. (2004). Powder-snow avalanches: Approximation as non-Boussinesq clouds with a Richardson number dependent entrainment func-tion. *Journal of Geophysical Research*, *109*(F1), F01005. https://doi.org/10.1029/2003jf000052

Andrews, B. J. (2014). Dispersal and air entrainment in unconfined dilute pyroclastic density currents. *Bulletin of Volcanology*, *76*(9), 852. https://doi.org/10.1007/s00445-014-0852-4

Bartelt, P., Bebi, P., Feistl, T., Buser, O., & Caviezel, A. (2018b). Dynamic magnification factors for tree blow-down by powder snow avalanche air blasts. *Natural Hazards and Earth System Sciences*, *18*(3), 759–764. https://doi.org/10.5194/nhess-18-759-2018

Bartelt, P., Buser, O., & Platzer, K. (2006). Fluctuation-dissipation relations for granular snow avalanches. *Journal of Glaciology*, *52*(179), 631–643. https://doi.org/10.3189/172756506781828476

Bartelt, P., Buser, O., Valero, C. V., & Bühler, Y. (2016). Configurational energy and the formation of mixed flowing/powder snow and ice avalanches. *Annals of Glaciology*, *57*(71), 179–188. https://doi.org/10.3189/2016aog71a464

Bartelt, P., Christen, M., Bühler, Y., & Buser, O. (2018a). Thermomechanical modelling of rock avalanches with debris, ice and snow entrainment. *Numerical Methods in Geotechnical Engineering*, *IX*, 1047–1054.

Bartelt, P., Christen, M., Bühler, Y., Caviezel, A., & Buser, O. (2018c). Snow entrainment: Avalanche interaction with an erodible substrate. *Proceedings, International Snow Science Workshop*, 16–720.

Bartelt, P., & McArdell, B. W. (2009). Granulometric investigations of snow avalanches. *Journal of Glaciology*, *55*(193), 829–833. https://doi.org/10.3189/002214309790152384

BFF/SLF (1984). *Richtlinien zur Berücksichtigung der Lawinengefahr bei raumwirksamen T ätigkeiten*. Bundesamt für Forstwesen/Eidgenössisches Institut für Schnee- und Lawinenforschung. (in German).

Bozhinskiy, A. N., & Losev, K. S. (1998). *The fundamentals of avalanche science: Davos* (Vol. 55). Eidgenös-sisches Institut für Schnee- und Lawinenforschung.

Brosch, E., Lube, G., Cerminara, M., Esposti-Ongaro, T., Breard, E. C. P., Dufek, J., et al. (2021). Destructiveness of pyroclastic surges controlled by turbulent fluctuations. *Nature Communications*, *12*(1), 7306. https://doi.org/10.1038/s41467-021-27517-9

Buser, O., & Bartelt, P. (2009). Production and decay of random kinetic energy in granular snow avalanches. *Journal of Glaciology*, *55*(189), 3–12. https://doi.org/10.3189/002214309788608859

Buser, O., & Bartelt, P. (2011). Dispersive pressure and density variations in snow avalanches. *Journal of Glaciology*, *57*(205), 857–860. https://doi.org/10.3189/002214311798043870

Buser, O., & Bartelt, P. (2015). An energy-based method to calculate streamwise density variations in snow avalanches. *Journal of Glaciology*, *61*(227), 563–575. https://doi.org/10.3189/2015jog14j054

Carroll, P. L., & Blanquart, G. (2013). A proposed modification to Lundgren's physical space velocity forcing method for isotropic turbulence. *Physics of Fluids*, *25*(10), 105114. https://doi.org/10.1063/1.4826315

Christen, M., Kowalski, J., & Bartelt, P. (2010). Numerical simulation of dense snow avalanches in three-dimensional terrain. *Cold Regions Science and Technology*, *63*(1–2), 1–14. https://doi.org/10.1016/j.coldregions.2010.04.005

Dreier, L., Bühler, Y., Ginzler, C., & Bartelt, P. (2016). Comparison of simulated powder snow avalanches with photogrammetric measurements. *Annals of Glaciology*, *57*(71), 371–381. https://doi.org/10.3189/2016aog71a532

Eckerstorfer, M., Bühler, Y., Frauenfelder, R., & Malnes, E. (2016). Remote sensing of snow avalanches: Recent advances, potential, and limitations. *Cold Regions Science and Technology*, *121*, 126–140. https://doi.org/10.1016/j.coldregions.2015.11.001

Fei, J. B., Liu, Z. K., & Jie, Y. X. (2022). Immiscible two-phase model for air blasts created during natural avalanches. *Geological Society of America Bulletin*, *135*, 2155–2176. https://doi.org/10.1130/b36411.1

Feistl, T., Bebi, P., Christen, M., Margreth, S., Diefenbach, L., & Bartelt, P. (2015). Forest damage and snow avalanche flow regime. *Natural Hazards and Earth System Sciences*, *15*(6), 1275–1288. https://doi.org/10.5194/nhess-15-1275-2015

Fujita, K., Inoue, H., Izumi, T., Yamaguchi, S., Sadakane, A., Sunako, S., et al. (2017). Anomalous winter-snow-amplified earthquake-induced disaster of the 2015 Langtang avalanche in Nepal. *Natural Hazards and Earth System Sciences*, *17*(5), 749–764. https://doi.org/10.5194/nhess-17-749-2017

Gorynina, O., & Bartelt, P. (2023). Powder snow avalanche impact on hanging cables. *Internal Journal of Impact Engineering*, *173*, 104422. https://doi.org/10.1016/j.ijimpeng.2022.104422

Hermann, F., & Hutter, K. (1991). Laboratory experiments on the dynamics of powder-snow avalanches in the run-out zone. *Journal of Glaciology*, *37*(126), 281–295. https://doi.org/10.1017/s0022143000007292

Issler, D. (1998). Modelling of snow entrainment and deposition in powder-snow avalanches. *Annals of Glaciology*, *26*, 256–258. https://doi.org/10.1017/s0260305500014919

Ito, Y., Naaim-Bouvet, F., Nishimura, K., Bellot, H., Thibert, E., Ravanat, X., & Fontaine, F. (2017). Measurement of snow particle size and velocity in avalanche powder clouds. *Journal of Glaciology*, *63*(238), 249–257. https://doi.org/10.1017/jog.2016.130

Ivanova, K., Caviezel, A., Bühler, Y., & Bartelt, P. (2022). Numerical modelling of turbulent geophysical flows using a hyperbolic shear shallow water model: Application to powder snow avalanches. *Computers & Fluids*, *223*, 105211. https://doi.org/10.1016/j.compfluid.2021.105211

Jonsson, M. J., Foetzki, A., Kalberer, M., Lundström, T., Ammann, W., & Stöckli, V. (2006). Root-soil rotation stiffness of Norway spruce (Picea abies (L.) Karst) growing on subalpine forested slopes. *Plant and Soil*, *285*(1–2), 267–277. https://doi.org/10.1007/s11104-006-9013-7

Kargel, J. S., Leonard, G. J., Shugar, D. H., Haritashya, U. K., Bevington, A., Fielding, E. J., et al. (2016). Geomorphic and geologic controls of geohazards induced by Nepal's 2015 Gorkha earthquake. *Science*, *373*(6269), 300–306. https://doi.org/10.1126/science.aac8353

Meister, R. (1995). Country-wide avalanche warning in Switzerland. In *Proceedings of the international snow science workshop*. In *Int. snow sci. workshop 1994 organ. comm* (pp. 58–71).

Nishimura, K., Sandersen, F., Kristensen, K., & Lied, K. (1995). Measurements of powder snow avalanche -Nature-. *Surveys in Geophysics*, *16*(5–6), 649–660. https://doi.org/10.1007/bf00665745

Richard, G. L., & Gavrilyuk, S. L. (2012). A new model of roll waves: Comparison with Brock's experiments. *Journal of Fluid Mechanics*, *698*, 374–405. https://doi.org/10.1017/jfm.2012.96

Richard, G. L., & Gavrilyuk, S. L. (2013). The classical hydraulic jump in a model of shear shallow-water flows. *Journal of Fluid Mechanics*, *75*, 492–521. https://doi.org/10.1017/jfm.2013.174

Salm, B. (1993). Flow, flow transition and runout distances of flowing avalanche. *Annals of Glaciology*, *18*, 221–226. https://doi.org/10.3189/s0260305500011551

Sampl, P., & Granig, M. (2009). *Avalanche simulation with SAMOS-AT* (pp. 519–523). Proc Int Snow Science Workshops.

Schweizer, J. (2008). Snow avalanche formation and dynamics. *Cold Regions Science and Technology*, *54*(3), 153–154. https://doi.org/10.1016/j.coldregions.2008.08.005

Sovilla, B., & Bartelt, P. (2002). Observations and modelling of snow avalanche entrainment. *Natural Hazards and Earth System Sciences*, *2*(3/4), 169–179. https://doi.org/10.5194/nhess-2-169-2002

Sovilla, B., McElwaine, J. N., & Köhler, A. (2018). The intermittency regions of powder snow avalanches. *Journal of Geophysical Research: Earth Surface*, *123*(10), 2525–2545. https://doi.org/10.1029/2018jf004678

Stoffel, L., Margreth, S., Schaer, M., Christen, M., Bühler, Y., & Bartelt, P. (2016). Powder snow avalanche engineering: New methods to calculate air-blast pressures for hazard mapping. In G. Koboltschnig (Ed.), *13th congress INTERPRAEVENT 2016. 30 May to 2 June 2016. Lucerne, Switzerland. Conference proceedings "Living with natural risks* (pp. 416–425).

Sukhanov, G. (1982). The mechanism of avalanche air blast formation as derived from field measurements. *Data Glaciology Student*, *44*, 94–98.

Sukhanov, G., & Kholobayev, P. (1982). Variability of avalanche air blast in time and space. *Data Glaciology Student*, *44*, 98–105.

Turnbull, B., & Bartelt, P. (2003). Mass and momentum balance model of a mixed flowing/powder snow avalanche. *Surveys in Geophysics*, *24*(5/6), 465–477. https://doi.org/10.1023/b:geop.0000006077.82404.84

Turnbull, B., & McElwaine, J. N. (2007). A comparison of powder-snow avalanches at Valle´e de la Sionne, Switzerland, with plume theories. *Journal of Glaciology*, *53*(180), 30–40. https://doi.org/10.3189/172756507781833938

Turnbull, B., McElwaine, J. N., & Ancey, C. (2007). Kulikovskiy–Sveshnikova–Beghin model of powder snow avalanches: Development and application. *Journal of Geophysical Research*, *112*(F1), F01004. https://doi.org/10.1029/2006jf000489

Valero, C. V., Jones, K. W., Bühler, Y., & Bartelt, P. (2015). Release temperature, snow-cover entrainment and the thermal flow regime of snow avalanches. *Journal of Glaciology*, *61*(225), 173–184. https://doi.org/10.3189/2015jog14j117

Veitinger, J., & Sovilla, B. (2016). Linking snow depth to avalanche release area size: Measurements from the Vallée de la Sionne field site. *Natural Hazards and Earth System Sciences*, *16*(8), 1953–1965. https://doi.org/10.5194/nhess-16-1953-2016

Zhuang, Y. (2023a). Air blast-tree breakage [Dataset]. Figshare. https://doi.org/10.6084/m9.figshare.23592693.v1

Zhuang, Y. (2023b). Improved RAMMS::Extended model to calculate the avalanche-induced air blast [Software]. RAMMS. http://ramms.slf.ch/en/modules/extended.html

Zhuang, Y., Xing, A. G., Bartelt, P., Bilal, M., & Ding, Z. W. (2023). Dynamic response and breakage of trees subject to a landslide-induced air blast. *Natural Hazards and Earth System Sciences*, *23*(4), 1257–1266. https://doi.org/10.5194/nhess-23-1257-2023

Zhuang, Y., Xu, Q., Xing, A. G., Bilal, M., & Gnyawali, K. R. (2023). Catastrophic air blasts triggered by large ice/rock avalanches. *Landslides*, *20*(1), 53–64. https://doi.org/10.1007/s10346-022-01967-8